Parallel Low-Loss Measurement of Multiple Atomic Qubits

Minho Kwon,* Matthew F. Ebert, Thad G. Walker, and M. Saffman
Department of Physics, University of Wisconsin-Madison, 1150 University Avenue, Madison, Wisconsin 53706, USA
(Received 27 June 2017; published 30 October 2017)

We demonstrate low-loss measurement of the hyperfine ground state of rubidium atoms by state dependent fluorescence detection in a dipole trap array of five sites. The presence of atoms and their internal states are minimally altered by utilizing circularly polarized probe light and a strictly controlled quantization axis. We achieve mean state detection fidelity of 97% without correcting for imperfect state preparation or background losses, and 98.7% when corrected. After state detection and correction for background losses, the probability of atom loss due to the state measurement is $< 2\%$ and the initial hyperfine state is preserved with $> 98\%$ probability.

DOI: 10.1103/PhysRevLett.119.180504

Experiments with qubits encoded in hyperfine states of neutral atoms are being actively developed as a route towards scalable quantum information processing [1]. Several research groups have demonstrated preparation and control of order 50 qubits in 1D [2], 2D [3,4], and 3D [5] optical lattices. Quantum computation requires qubit state measurements to determine the result of a computation, and for measurement based quantum error correction [6]. Measurement of the quantum state of an atomic hyperfine qubit is most often performed by using a cycling, or near cycling, transition which repetitively transfers the qubit between a bright state $|B\rangle$ and an excited state $|e_B\rangle$. Detection of scattered photons due to illumination with light that is near resonant with the cycling transition projects the qubit into state $|B\rangle$. Conversely, if no photons are detected, the qubit is projected into the dark state $|D\rangle$. This idealized picture breaks down if the cycling transition is not perfectly closed, in which case an atom in state $|B\rangle$ may suffer a Raman transition to $|D\rangle$, thereby giving a measurement error.

Measurements that use a cycling transition rely on the availability of a metastable qubit dark state $|D\rangle$, or on shelving one of the qubit levels into a metastable dark state, as is done in trapped ion experiments [7]. In alkali atom experiments with qubits encoded in ground hyperfine levels the availability of a cycling transition generally relies on an angular momentum selection rule that is enforced by using probe light with a well-defined polarization. This implies that the probe light propagates along a single axis in space, which results in atomic heating due to the random direction of scattered photons. For a lossless measurement either the potential confining the atom should be sufficiently deep for the heating to be tolerable, as in experiments with ions [8], or the detection system should allow for a state measurement after scattering only a small number of photons to minimize heating. This latter approach was demonstrated with optically trapped atomic qubits [9–11] using single photon detectors.

There are several possible alternative measurement approaches including coupling of an atom to a high finesse cavity which enables state detection with minimal heating and without loss of atoms [12–14]. Superlattices with spin dependent potentials have been used for parallel measurement of atomic spin states [15]. It has been proposed to perform fast state measurements by coupling a single atom to a many atom ensemble, as a means of increasing the effective photon scattering rate [16]. It is also possible to enforce a dark state condition with three-dimensional probing light that cools the atoms, but this requires an inconvenient sequence of shelving steps [17].

In order to take full advantage of the large number of qubits available in neutral atom experiments, it is desirable to be able to losslessly measure multiple qubits in parallel. This can be done by imaging scattered light from an array of qubits onto a sensitive imaging detector such as an electron multiplying charge coupled device (EMCCD) camera. Although EMCCD cameras have high quantum efficiency, they suffer from excess readout noise which has hitherto rendered parallel lossless state detection infeasible. To circumvent this limitation previous array experiments used a "blow away" technique where atoms in $|B\rangle$ are ejected from the array using a single unbalanced beam, followed by detection of the presence or absence of an atom. Atom detection is performed using a 3D light field that cools the atoms, but does not prevent state changing Raman transitions during the measurement. This approach provides state measurements, but requires that a new atom has to be reloaded, half the time on average, which severely impacts the experimental data rate.

In this Letter we show that low-loss state detection of multiple atomic qubits is possible in parallel using an EMCCD camera. This requires a careful choice of parameters to minimize both the motional heating rate (which is lower at large detuning) and the Raman depumping rate (which is lower at small detuning). The enabling advances include use of a moderately high numerical aperture (NA = 0.4) collection lens, deep optical traps, and careful preparation of the polarization state of the probe light to minimize Raman transitions from $|B\rangle \rightarrow |D\rangle$.

The detection method is compatible with an ideal, projective measurement of the quantum state that leaves the atom in an eigenstate of $\hat{\sigma}_z$ (for neutral atom qubits a state of definite $|F, M_F\rangle$). Observation of the dark state $|D\rangle$ leaves the atomic state unchanged. If the bright state is encoded in $|F_+, M_F\rangle$, with F_+ the upper hyperfine state, observation of the bright state $|B\rangle$ leaves the atom in $|F_+, F_+\rangle$ for any initial M_F. The qubit can then be restored to $|F_+, M_F\rangle$ by following the detection of $|B\rangle$ with a sequence of rotations using stimulated Raman transitions or microwave pulses. The measurement can also be made cross talk free, a requirement for quantum error correction [18]. We emphasize that the experimental approach is compatible with quantum gate experiments in qubit registers [1], with no changes to the experimental apparatus. Since EMCCD cameras are available with up to 10^6 pixels the method demonstrated here has the potential for scaling to large arrays with thousands of atomic qubits. Similar results to ours have been independently reported in Ref. [22].

The experimental geometry and measurement sequence are shown in Fig. 1. Atoms are prepared in the $|F = 1\rangle$ or $|F = 2\rangle$ hyperfine levels of the ^{87}Rb $5s_{1/2}$ electronic ground state, corresponding to $|D\rangle$ and $|B\rangle$, respectively. Although qubits are defined in terms of specific hyperfine-Zeeman states $|1\rangle = |F_1, M_{F1}\rangle$ and $|0\rangle = |F_0, M_{F0}\rangle$ we use $|B\rangle$ and $|D\rangle$ here to represent random mixtures of the M_F states of the $F = 2$ and $F = 1$ hyperfine levels, respectively. The demonstration of measurement of states $|B\rangle$ and $|D\rangle$ also applies, without modification, to any pair of hyperfine-Zeeman states as long as they are attached to different hyperfine levels.

To prepare states of single atoms we start with a standard magneto-optical trap (MOT) that is then overlapped with a 1D array of five optical dipole traps (ODTs) formed by focusing 1040 nm light to a waist of w $\simeq 2.5$ μm. The traps are (2.8, 4.4, 5.6, 3.9, 3.4) mK deep and are spaced by $\sim$9 μm. The traps are pencil shaped with atomic density distributions of size (standard deviations) $\Delta_z, \Delta_r \sim 7.0, 0.7$ μm, with the long axis along the optical axis of the collection optics. Single atoms are loaded with probability 20%–30% at a temperature of $\sim$100 μK.

In order to measure the initial trap populations, the atoms are probed using 6 MOT beams with components near-resonant with $|B\rangle \leftrightarrow |e_B\rangle$ and $|D\rangle \leftrightarrow |e_D\rangle$ simultaneously, where $|e_B\rangle$ is the $F' = 3$ level and $|e_D\rangle$ is the $F' = 2$ level of the $5p_{3/2}$ excited state. Atom fluorescence is collected by a NA $= 0.4$ lens, and imaged onto an EMCCD camera (Andor iXon EM + DU-860). The magnification was chosen such that the site separation is 2 pixels, and the signal from each ODT is integrated over a region of interest (ROI) defined by 5 camera pixels, as shown in Fig. 2(a). We image each atom onto only a few pixels to minimize the electronic background noise incurred during camera readout. The excited states, $|e_B\rangle, |e_D\rangle$, are antitrapped in the ODT, so to avoid heating the atom we toggle the ODT and

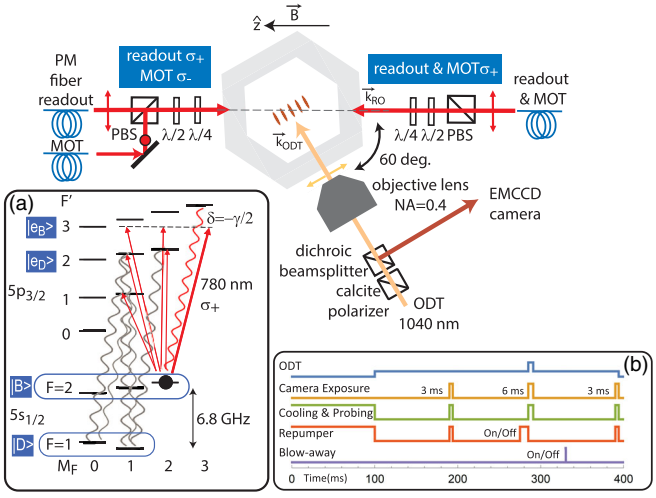

FIG. 1. Experimental setup around the hexagonal vacuum cell. For state readout σ_+ polarized light propagates along $\pm\vec{k}_{\mathrm{RO}}$, which is parallel to the quantization axis defined by the bias magnetic field $\vec{B}$. The trap light propagates along $\vec{k}_{\mathrm{ODT}}$ and a dichroic beam splitter separates the trap light and fluorescence light which is imaged onto the camera. Inset (a) shows the levels used for readout including the bright $|B\rangle$ and dark $|D\rangle$ hyperfine levels, and the corresponding excited state levels $|e_B\rangle$, $|e_D\rangle$. Inset (b) shows the experimental timing diagram.

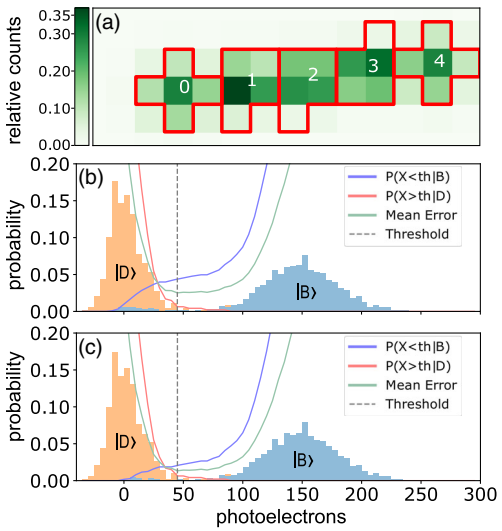

FIG. 2. (a) Regions of interest are five pixels enclosed by red borders with the relative photon counts on each pixel shown by the green shading. Each 5 pixel ROI receives (76,88,89,92,76)% of the light from the corresponding trapped atom. Neighboring site fluorescence cross talk is $\sim$2%. Each pixel represents a 4 μm $\times$ 4 μm area and the site-to-site separation is $\sim$9 μm. (b) Histograms of nondestructive readout in the central region (#2) for initial states $|B\rangle$ and $|D\rangle$. (c) The same data set postselected on the presence of an atom in the ROI in the third measurement, leaving only Raman depumping and state preparation as sources of error. Signals in histograms are background subtracted.

the probe beams out of phase with a 50% duty cycle at 1.25 MHz. The photon detection efficiency is estimated to be (1.6%–2.0%), accounting for the lens solid angle and dipole emission pattern (3.9%), transmission through optics (74%), EMCCD quantum efficiency ($\eta = 75\%$), and fluorescence lying outside of the camera pixels used to define regions of interest (76%–92%).

Upon completion of the population measurement, there is a 100 ms delay for image transfer to the computer, after which the atoms are initialized in a random superposition of the Zeeman substates of one of the hyperfine levels, chosen by leaving either $|D\rangle \leftrightarrow |e_D\rangle$ or $|B\rangle \leftrightarrow |e_B\rangle$ on to depopulate the coupled state. To prevent leakage light from disrupting the initialized states mechanical shutters block unwanted light after initialization is completed. We estimate the state preparation fidelity for both states to be $> 99.5\%$, limited by the fidelity of blow away measurements that are performed at reduced ODT depth.

After state initialization, a bias magnetic field $B_z \sim 20$ G making an angle of 60° from $\vec{k}_{\mathrm{ODT}}$, the long axis of the ODTs, is switched on. The probe beams propagate along and counter to $\vec{k}_{\mathrm{RO}}$, which is set to be parallel to $\hat{z}$ with a possible small alignment error θ. We use counterpropagating probe beams to mitigate the effect of heating due to near-resonant radiation pressure. In order to suppress Raman transitions both readout beams are σ_+ polarized which optically pumps the atoms into the lower state of the $|2,2\rangle \leftrightarrow |3',3'\rangle$ cycling transition. The counterpropagating probe beams are generated from separate lasers with a relative frequency offset of 500 kHz. This technique avoids standing wave patterns, which can cause a time dependent drift in the single atom scattering rate thereby broadening the camera signal distribution. During the state measurement sequence the trap depths are temporarily doubled to enhance retention of the atoms. The probe beams are set to saturation parameter $s_0 = 1$ (summed over both beams) and detuning $\delta = -(\gamma/2)$ red of the Zeeman shifted $|2,2\rangle \leftrightarrow |3',3'\rangle$ transition to provide maximal motional damping [23] with γ the excited state linewidth. The atoms are illuminated for 6 ms with the same 50% duty cycle as is used for the population measurement and fluorescence light is collected by the EMCCD for analysis. The resulting data are shown in Fig. 2. The hyperfine state is determined on the basis of a simple threshold condition relative to the vertical dashed lines in Figs. 2(b),2(c). Although more extensive analysis that utilizes information gained from the temporal or spatial distribution of light in each ROI can further reduce uncertainties [7,22], our results show that the threshold condition alone is adequate for high fidelity measurements.

After an additional 100 ms delay for image transfer, a third readout sequence probes the atoms again. Depending on the experiment, the third readout is either a second population measurement for probing atom loss or a destructive state selective measurement using a blow away beam for measuring the number of atoms depumped from $|B\rangle$ to $|D\rangle$. Full characterization of the nondestructive measurement requires 4 experiments: 2 (state preparation $|B\rangle$ or $|D\rangle$) ×2 (blow away on or off). The results of the 4 experiments are summarized in Table I for the center site and Table II for the other sites. We note that the results marked with (a) include 2% atom loss between each camera readout due to the finite trap lifetime $\tau \sim 5$ s and the 100 ms gap between each measurement. The background collision loss is not a fundamental limitation, and could be reduced by decreasing the chamber pressure or by shortening the image transfer time.

TABLE I. Results in the central site (#2) averaged over 2000 measurements. Data marked (a) are without correction, and data marked (b) are postselected on the presence of an atom in the ROI in the third measurement, leaving only Raman depumping and state preparation as sources of error. The final state results are found from a third, state-selective measurement using a blow away beam.

	Detected state (%)		Final state (%)		
Initial state	$\|B\rangle$	$\|D\rangle$	$\|B\rangle$	$\|D\rangle$	Lost
$\|B\rangle$	(a) 95.6(6)	(a) 4.4(6)	98.6(1.9)	0.6 (1.6)	0.8(1.3)
	(b) 98.0(4)	(b) 2.0(4)			
$\|D\rangle$	0.6(4)	99.4(4)	N/A	99.6(1.6)	0.4 (1.6)

The primary limitation to the nondestructive measurement is the mean number of photons N_γ that can be scattered before the atom is depumped from $|B\rangle$ to $|D\rangle$. When using random polarization $N_\gamma = 38\,340/(1 + 4\delta^2/\gamma^2 + s_0)$, where $s_0 = I/I_{\mathrm{s,eff}}$ and $I_{\mathrm{s,eff}} = 3.6$ mW/cm^2 is the saturation parameter for randomly polarized light; see Ref. [18] for a derivation. With typical experimental parameters 10^4 photons could be scattered, which would lead to approximately 100 photoelectrons, which is technically enough to clearly resolve the $|B\rangle$ and $|D\rangle$ photon histograms. However, the $|B\rangle$ state histogram would leave a long tail from depumping events during the exposure that would overlap with the $|D\rangle$ state distribution. Therefore, in order to obtain clearly distinguishable photoelectron statistics we need the additional constraint that atoms scatter $\sim 10^4$ photons with minimal depumping, a condition that isotropic polarization does not satisfy.

TABLE II. Loss-corrected detection fidelities for the outer four traps. $|\psi\rangle_i$ is the prepared state.

	Detection fidelity (%)			
ROI	No. 0		No. 1	
$\|\psi\rangle_i$	$\|B\rangle$	$\|D\rangle$	$\|B\rangle$	$\|D\rangle$
$\|B\rangle$	97.1(5)	2.9(5)	98.3(3)	1.7(3)
$\|D\rangle$	0(0)	100(0)	1.0(5)	99.0(5)
	No. 3		No. 4	
$\|\psi\rangle_i$	$\|B\rangle$	$\|D\rangle$	$\|B\rangle$	$\|D\rangle$
$\|B\rangle$	97.7(6)	2.3(6)	98.2(1.2)	1.8(1.2)
$\|D\rangle$	0.5(4)	99.5(4)	0	100(0)

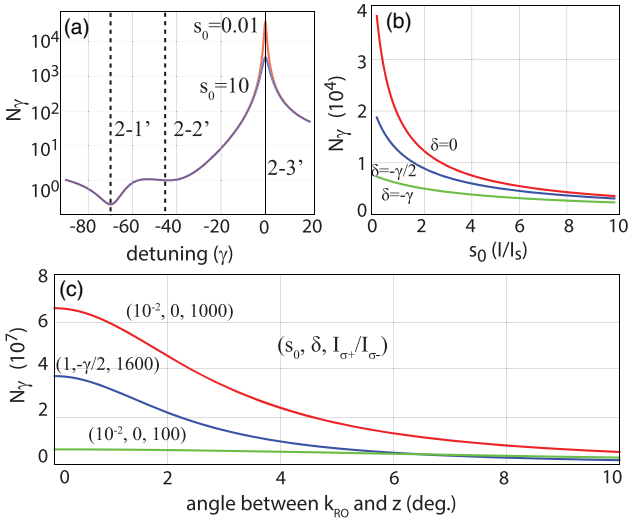

FIG. 3. Dependence of the mean number of resonant photons per Raman photon on probe light parameters. (a) Detuning dependence spanning neighboring levels. (b) Intensity dependence at three different detunings. (c) Enhancement with σ polarized light for given saturation, detuning, and intensity contrast $I_{\sigma_+}/I_{\sigma_-}$ between σ_+ and σ_-.

To suppress the depumping we have used σ_+-polarized light along the quantization axis to pump the atoms into $|2,2\rangle$, the lower level of the cycling transition as described above. In an actual experiment there is still a finite depumping rate due to polarization impurity or a small angular mismatch θ between $\hat{z}$, the direction of the magnetic field, and $\vec{k}_{\mathrm{RO}}$, the axis of the readout beams. The figure of merit is the number of photons that the bright state can scatter before it falls into the dark state, as shown in Fig. 3. We can quantify the probability of depumping by summing the rates over Raman depumping channels and comparing to the scattering rate on the cycling transition [18]. We estimate that we are able to scatter $N_{\gamma,\sigma} = 3.7 \times 10^5$ photons corresponding to an enhancement factor of $\sim$20 over the unpolarized case with parameters $s_0 = 1$, $\delta = -\gamma/2$ and measured polarization purity $I_{\sigma_+}/I_{\sigma_-} = 1600$ [18]. There is also a small transient contribution to the depumping probability as the atoms are pumped from the initial state towards $|2,2\rangle$, which is estimated in Ref. [18].

It is also necessary to account for depumping due to the vector and tensor light shifts imposed by the ODT. Circular polarization of the ODT light results in a vector shift on the atoms which adds a fictitious magnetic field, $\vec{B}_{\mathrm{fict}}$, along $\vec{k}_{\mathrm{ODT}}$. The 60° angle between $\vec{k}_{\mathrm{ODT}}$ and $\vec{k}_{\mathrm{RO}}$ drives Larmor precession, which reopens the depumping channels. In terms of the trap depth U_0 the fictitious field is $\vec{B}_{\mathrm{fict}}/U_0 = 29.77\mathcal{A}\alpha^{(1)}_{|B\rangle}\hat{k}_{\mathrm{ODT}}/\alpha^{(0)}_{|B\rangle}$ (G/mK) [18], with $\alpha^{(0)}_{|B\rangle}$, $\alpha^{(1)}_{|B\rangle}$ the scalar and vector polarizabilities, and $-1 \leq \mathcal{A} \leq 1$ the degree of circular polarization. For our experimental parameters, $\mathcal{A} \sim 2 \times 10^{-4}$, $\lambda_{\mathrm{ODT}} = 1040$ nm, $\vec{B}_{\mathrm{fict}}/U_0 = 0.3$ mG/mK. To mitigate depumping from $\vec{B}_{\mathrm{fict}}$ we used a bias field of $B_z \sim 20$ G, such that the depumping rate was independent of ODT power [18], which shows that the vector light shift did not cause additional depumping for our parameters.

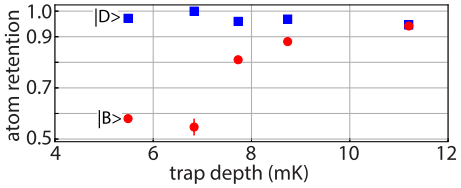

FIG. 4. Probability of atom retention after nondestructive readout as a function of trap depth during the readout phase. Background gas collisions cause $\sim$4% atom loss between the first and third measurements.

In addition, excited state tensor light shifts couple M'_F states, creating a new set of energy eigenstates that are superpositions of $|F', M'_F\rangle$ states, which breaks the cycling character of the $|2,2\rangle \leftrightarrow |3',3'\rangle$ transition. To avoid tensor shifts during readout the probe and ODT lights are chopped out of phase so that the excited state is never populated when the ODT is on.

Despite the use of counterpropagating σ_+ beams, heating was still noticeable, limiting atom retention after the measurement, as is shown in Fig. 4, and forcing us to use traps that are $\sim$10 mK deep. This limited performance may be attributed to laser intensity noise, lack of sub-Doppler cooling mechanisms, and 1D cooling. Future improvements including working with a higher NA lens to improve photon collection efficiency, and cooling the atoms into the Lamb-Dicke regime to suppress recoil heating will further reduce atom loss. Using blue detuned traps with intensity minima at the location of the atoms, as in Refs. [5,24], would reduce the excited state tensor mixings, and obviate the need to turn the ODT on and off, thereby reducing any heating due to trap switching.

In conclusion, we have demonstrated nondestructive parallel readout of an array of five Rb atoms. Increasing the collection efficiency of the imaging optics, combined with colder atoms, and possibly more refined analysis of the spatial information provided by the camera, we anticipate that loss of atoms due to heating can be reduced to a level compatible with implementation of repetitive error correction for quantum computation.

This work was supported by NSF Grant No. 1521374, the AFOSR Quantum memories MURI, and the ARL-CDQI through cooperative agreement W911NF-15-2-0061. M. S. thanks Dieter Meschede for sharing their results prior to publication.

*mkwon22@wisc.edu

[1] M. Saffman, Quantum computing with atomic qubits and Rydberg interactions: Progress and challenges, J. Phys. B **49**, 202001 (2016).

[2] M. Endres, H. Bernien, A. Keesling, H. Levine, E. R. Anschuetz, A. Krajenbrink, C. Senko, V. Vuletic, M. Greiner, and M. D. Lukin, Atom-by-atom assembly of defect-free one-dimensional cold atom arrays, Science **354**, 1024 (2016).

[3] T. Xia, M. Lichtman, K. Maller, A. W. Carr, M. J. Piotrowicz, L. Isenhower, and M. Saffman, Randomized Benchmarking of Single-Qubit Gates in a 2D Array of Neutral-Atom Qubits, Phys. Rev. Lett. **114**, 100503 (2015).

[4] D. Barredo, S. de Leséleuc, V. Lienhard, T. Lahaye, and A. Browaeys, An atom-by-atom assembler of defect-free arbitrary two-dimensional atomic arrays, Science **354**, 1021 (2016).

[5] Y. Wang, A. Kumar, T.-Y. Wu, and D. S. Weiss, Single-qubit gates based on targeted phase shifts in a 3D neutral atom array, Science **352**, 1562 (2016).

[6] S. J. Devitt, W. J. Munro, and K. Nemoto, Quantum error correction for beginners, Rep. Prog. Phys. **76**, 076001 (2013).

[7] A. H. Myerson, D. J. Szwer, S. C. Webster, D. T. C. Allcock, M. J. Curtis, G. Imreh, J. A. Sherman, D. N. Stacey, A. M. Steane, and D. M. Lucas, High-Fidelity Readout of Trapped-Ion Qubits, Phys. Rev. Lett. **100**, 200502 (2008).

[8] H. Häffner, C. F. Roos, and R. Blatt, Quantum computing with trapped ions, Phys. Rep. **469**, 155 (2008).

[9] M. J. Gibbons, C. D. Hamley, C.-Y. Shih, and M. S. Chapman, Nondestructive Fluorescent State Detection of Single Neutral Atom Qubits, Phys. Rev. Lett. **106**, 133002 (2011).

[10] A. Fuhrmanek, R. Bourgain, Y. R. P. Sortais, and A. Browaeys, Free-Space Lossless State Detection of a Single Trapped Atom, Phys. Rev. Lett. **106**, 133003 (2011).

[11] Y.-Y. Jau, A. M. Hankin, T. Keating, I. H. Deutsch, and G. W. Biedermann, Entangling atomic spins with a Rydberg-dressed spin-flip blockade, Nat. Phys. **12**, 71 (2016).

[12] J. Bochmann, M. Mücke, C. Guhl, S. Ritter, G. Rempe, and D. L. Moehring, Lossless State Detection of Single Neutral Atoms, Phys. Rev. Lett. **104**, 203601 (2010).

[13] J. Volz, R. Gehr, G. Dubois, J. Estève, and J. Reichel, Measurement of the internal state of a single atom without energy exchange, Nature (London) **475**, 210 (2011).

[14] H. Zhang, R. McConnell, S. Ćuk Q. Lin, M. H. Schleier-Smith, I. D. Leroux, and V. Vuletić, Collective State Measurement of Mesoscopic Ensembles with Single-Atom Resolution, Phys. Rev. Lett. **109**, 133603 (2012).

[15] M. Boll, T. A. Hilker, G. Salomon, A. Omran, J. Nespolo, L. Pollet, I. Bloch, and C. Gross, Spin- and density-resolved microscopy of antiferromagnetic correlations in Fermi-Hubbard chains, Science **353**, 1257 (2016).

[16] M. Saffman and T. G. Walker, Entangling single- and N-atom qubits for fast quantum state detection and transmission, Phys. Rev. A **72**, 042302 (2005).

[17] I. I. Beterov and M. Saffman, Rydberg blockade, Förster resonances, and quantum state measurements with different atomic species, Phys. Rev. A **92**, 042710 (2015).

[18] See Supplemental Material at http://link.aps.org/supplemental/10.1103/PhysRevLett.119.180504 for analysis of qubit shelving, photoelectron statistics, camera noise, and atomic state dynamics with dependencies on experimental parameters. The Supplemental Material includes Refs. [3,17,19–21].

[19] M. Hirsch, R. J. Wareham, M. L. Martin-Fernandez, M. P. Hobson, and D. J. Rolfe, A stochastic model for electron multiplication charge-coupled devices—from theory to practice, PLoS One **8**, 1 (2013).

[20] A. Hyvärinen and E. Oja, Independent component analysis: algorithms and applications, Neural Netw. **13**, 411 (2000).

[21] M. Martínez-Dorantes, Ph.D. thesis, Rheinischen Friedrich-Wilhelms-Universität Bonn, 2016.

[22] M. Martinez-Dorantes, W.Alt, J. Gallego, S. Ghosh, L. Ratschbacher, Y. Völzke, and D. Meschede, Nondestructive Parallel Readout of Neutral Atom Registers in Optical Potentials, proceeding Letter, Phys. Rev. Lett. **119**, 180503 (2017).

[23] D. J. Wineland and W. M. Itano, Laser cooling of atoms, Phys. Rev. A **20**, 1521 (1979).

[24] M. J. Piotrowicz, M. Lichtman, K. Maller, G. Li, S. Zhang, L. Isenhower, and M. Saffman, Two-dimensional lattice of blue-detuned atom traps using a projected Gaussian beam array, Phys. Rev. A **88**, 013420 (2013).

Supplementary Material for Parallel low-loss measurement of multiple atomic qubits

Minho Kwon,* Matthew F. Ebert, Thad G. Walker, and M. Saffman
Department of Physics, University of Wisconsin-Madison,
1150 University Avenue, Madison, Wisconsin 53706
(Dated: September 22, 2017)

This supplementary material provides additional technical details for low loss measurement of atomic qubits.

CONTENTS

I. SHELVING FOR SINGLE SITE READOUT

Measurement based protocols for quantum error correction require that individual ancilla qubits can be measured without introducing crosstalk that changes the quantum state of data qubits. The low-loss measurement described in the main text does not satisfy this requirement since scattered photons may be absorbed by other, nearby atoms. This problem can be solved by shelving nearby atoms into dark states as described in Fig. 8 of [1]. The protocol described in [1] uses a shelving state that is not compatible with the measurement protocol in the main text of this paper. In Fig. 1 we describe a modified shelving method that is directly compatible with the measurement protocol demonstrated in the main text.

As shown in Fig. 1a)-d) we consider a register of qubits with the qubit to be measured indicated by a filled circle,

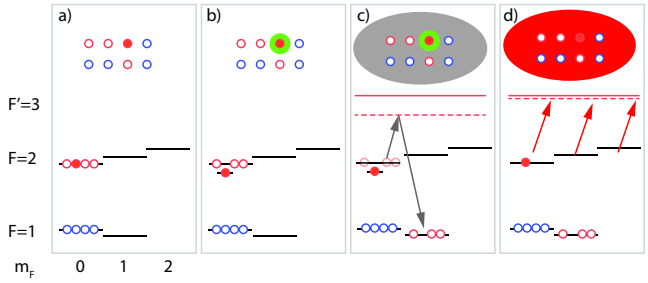

FIG. 1. Site-specific qubit readout with low crosstalk using shelving. a) Quantum register in arbitrary configuration. The solid circle is an ancilla qubit to be measured. Unfilled circles are qubits that will not be measured. b) A localized beam(green circle) introduces an ac Stark shift on the qubit to be measured. c) A global Raman beam or microwave resonant with the unshifted $|2,0\rangle \rightarrow |1,1\rangle$ transition applies a π pulse to coherently shelve the upper qubit state to $|1,1\rangle$ on all qubits that are not measured. d) Global σ_+ state-selective readout beams interrogate the unshelved atom as described in the main text. After the measurement the Stark shift beam is turned on again and all unmeasured atoms are returned to the qubit basis (see text for details).

and the qubits whose state should not be measured indicated by unfilled circles. A focused near-resonant beam is used to Stark shift the $|2,0\rangle$ state of the qubit to be measured. A global beam that addresses all qubits in the register is then used to transfer all atoms, except the Stark shifted one, from $|2,0\rangle \rightarrow |1,1\rangle$ via a stimulated Raman process timed to give a π pulse. Alternatively the two-photon Raman transition could be replaced by a one-photon microwave transition, as was demonstrated in [2]. After these shelving steps the qubit to be measured is interrogated with σ_+ polarized light as described in the main text.

After the qubit measurement the selected atom is left in the qubit basis state $|1,0\rangle$ if the measurement result was "0", or in the state $|2,2\rangle$ if the result was "1". If the measurement result was "0" the Raman or microwave fields are applied globally with a phase set to give a $-\pi$ pulse on the $|1,1\rangle \rightarrow |2,0\rangle$ transition. This restores all unmeasured register qubits to their original states and leaves the measured qubit in the basis state $|1,0\rangle$.

If the measurement result was "1" the measured qubit is in state $|2,2\rangle$ which is not resonant with the shelving beams. The unmeasured qubits are then restored to

* mkwon22@wisc.edu

their initial states as described in the preceding paragraph. The measured qubit is returned to the basis state $|2,0\rangle$ by the transitions $|2,2\rangle \rightarrow |1,1\rangle \rightarrow |2,0\rangle$ using either focused Raman light or a combination of a global microwave and a focused Stark shifting beam. When the measurement result is "1" there is an additional requirement that should be taken into account. When the qubit quantization axis is not parallel with $\vec{k}_{\mathrm{RO}}$, the propagation axis of the readout beams, the measurement leaves the atom in the state $|2,2\rangle$ with respect to quantization along $\vec{k}_{\mathrm{RO}}$. To restore the atom to the qubit state $|2,0\rangle$ the Raman transitions must provide a state rotation that corrects for the change of basis. In addition qubits shelved in $|1,1\rangle$ will acquire a relative phase between the $|1,1\rangle$ and $|1,0\rangle$ states. This phase must be compensated before restoring the qubits to the original basis states. This can be incorporated into the restoration pulses, or the phase can be cancelled using a magnetic field ramp opposite to that used during the measurement. Alternatively, these complications can be bypassed by using readout beams that have $\vec{k}_{\mathrm{RO}}$ parallel to the qubit quantization axis.

The single site measurement procedure described here can be extended in a natural way to simultaneous measurement of several sites provided that local Stark shifts are applied to each of the measured sites to prevent those atoms from being shelved. In this way multiple ancilla qubits can be measured in parallel as part of a quantum error correction sequence.

II. FLUORESCENCE STATISTICS WITH ATOM LOSS

With no loss mechanisms, the camera signal distributions for the cases of bright $|B\rangle$ and dark $|D\rangle$ states after probing for a time t are given by Poissonian distributions with means

$$\begin{aligned} \mu_D(t) &= (\gamma_D + \gamma_{bg})t + \mu_{CIC}, \\ \mu_B(t) &= (\gamma_B + \gamma_{bg})t + \mu_{CIC}, \end{aligned} \tag{1}$$

where γ_{bg}, γ_D, and γ_B are the background, dark state, and bright state photo-electron production rates and μ_{CIC} is the background photo-electron rate due to clock induced charge (CIC). CIC is a Poissonian noise source intrinsic to EMCCD cameras and is independent of the exposure time. It is discussed in more detail in the next section. The photo-electron production rate from $|D\rangle$, given by γ_D, is negligible compared to γ_B and γ_{bg}, therefore we set $\gamma_D = 0$ for this section and consider the dark state distribution as a background distribution for the bright state. Both the large average number of photo-electrons, $\mu_D \sim 100$, and fluctuations in probe intensity and detuning broaden the expected single-atom signal. Therefore we can treat the photo-electron distributions, $S_B(s)(S_D(s))$, as Gaussian: $G(s,\mu,\sigma) = (2\pi\sigma^2)^{-1/2} e^{-(s-\mu)^2/2\sigma^2}$. For our system, the effect of spurious noise from CIC is lower than other sources of background $\gamma_{bg} t > \mu_{CIC}$ for our exposure times, therefore we can simplify the analysis by assuming a Gaussian distribution for all noise sources, see Fig 2. The width of the distributions, $\sigma_B(\sigma_D)$, are determined experimentally by fitting the distributions given by

$$\begin{aligned} S_D(s) &= G(s, \mu_D, \sigma_D), \\ S_B(s) &= G(s, \mu_B, \sqrt{\sigma_B^2 + \sigma_D^2}), \end{aligned} \tag{2}$$

to the relevant camera signal distributions with no loss. The width of the background must be deconvolved from the width of the bright state distribution to correctly include the effect of losses during the measurement, although typically $\sqrt{\sigma_B^2 + \sigma_D^2} \approx \sigma_B$. For $|B\rangle$ a lossless measurement can be done by leaving the $|D\rangle \leftrightarrow |e_D\rangle$ hyperfine repumping light on during the camera exposure.

When losses during readout are included the bright state distribution, $S_B(s)$, changes from Gaussian to something more complicated. If the atom in $|B\rangle$ is lost or depumped into $|D\rangle$ at time $t' < t$, then the atom will cease scattering photons and will only accumulate photo-electrons at γ_{bg} for a time $t - t'$. Therefore the mean signal for an atom initially in $|B\rangle$ undergoing a loss event at time t' is given by $\mu_B^\star(t') = \gamma_B t' + \gamma_{bg} t + \mu_{CIC}$. This effectively adds a tail to the ideal Gaussian distribution. The normalized tail distribution, $S_B^\star$, is given by

$$S_B^\star = \left(\frac{\alpha}{1 - e^{\alpha t}}\right) \int_0^t dt' e^{-\alpha t'} G(s, \mu_B^\star(t'), \sigma_B^\star(t')), \tag{3}$$

where α is the combined heating induced loss and depumping rate and $\sigma_B^\star(t') \equiv \sqrt{\sigma_B^2(t'/t) + \sigma_D^2}$. To the best of our knowledge, this integral cannot be solved analytically unless $\sigma_{bg} = 0$. For simplicity we also set $\gamma_{bg}, \mu_{CIC} = 0$ and Eq. (3) becomes

$$S_B^\star \simeq \frac{\alpha}{2(1 - e^{-\alpha t})} \sqrt{\frac{t}{\chi}} e^{s\gamma_B t/\sigma_B^2} \left[A_+ - A_-\right], \tag{4}$$

where $\chi \equiv \gamma_B^2 t + 2\alpha\sigma_B^2$ and

$$A_\pm \equiv e^{\pm(s/\sigma_B^2)\sqrt{\chi t}} \left[\mathrm{erf}\left(\frac{s \pm \sqrt{\chi t}}{\sqrt{2}\sigma_B}\right) - 1\right].$$

The original distribution with finite background can be recovered by convolving $S_B^\star$ with the background distribution $G(s, \gamma_{bg} t + \mu_{CIC}, \sigma_D)$. In the case of small loss this is a small effect and the time-intensive convolution operation is not necessary.

The full camera signal distribution model, S_B, can be obtained now by a weighted sum of the distribution with no loss, $S_B^{(0)} \equiv G(s, \mu_B, \sigma_B)$, and the tail distribution with a loss event, $S_B^\star$:

$$S_B(s) = e^{-\alpha t} S_B^{(0)}(s) + (1 - e^{-\alpha t}) S_B^\star(s) \tag{5}$$

An example histogram for $|B\rangle$ is shown under conditions of large depumping losses (yellow) compared to no depumping loss (blue) in Fig 3.

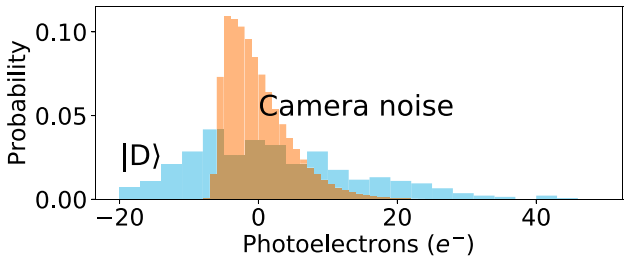

FIG. 2. A comparison of the intrinsic camera noise in the 5 pixel region of interest (ROI) with the camera shutter closed (yellow), and the photo-electron distribution for $|D\rangle$ (blue). The data are centered about the mean of the distribution. Intrinsic camera noise is $\sim 22(e^-)^2$, while the dark state has variance of $\sim 196(e^-)^2$, due to additional noise in the experimental setup.

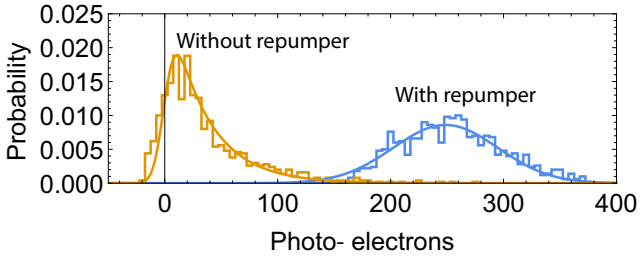

FIG. 3. Signal from a $t = 4$ ms exposure of $|B\rangle$ with isotropic polarization, detuning $\delta \sim -1.5\gamma$, and intensity $s_0 \sim 10$, with (blue) and without (yellow) the extra $|D\rangle \leftrightarrow |e_D\rangle$ hyperfine repumping light. The blue solid line is a fit to a Gaussian distribution with no loss, and is used to extract parameters for the fit to the yellow curve. The yellow curve is a fit for the loss rate α in Eq. (5) convolved with the background Gaussian distribution, all other parameters are fixed. The result of the fit yields a depumping rate of $\alpha = 1.8(1)$ ms^{-1}. The large loss rate for the case of isotropic polarization emphasizes the necessity of strict polarization control.

III. CAMERA NOISE

EMCCD cameras have multiple sources of noise which broaden the camera count distribution including dark counts, CIC, EM gain register noise, and analog to digital converter (ADC) noise. Modeling is possible though complicated[3]. Cooling the detector to -70 C reduces dark counts to a rate that is negligible on the scale of our $t < 10$ ms camera exposures. CIC is a Poissonian process, caused by impact ionization when reading out camera pixels, that gives the background photo-electron signal a long tail, see Fig 2. The long CIC tail is independent of exposure time and therefore sets a limit on how many photo-electrons must be collected to make a high fidelity threshold-based measurement. CIC events should lack any spatial correlation with photo-electron events, so the effect could be reduced further by including spatial information, such as an auto-correlation, into a multi-dimensional threshold cut.

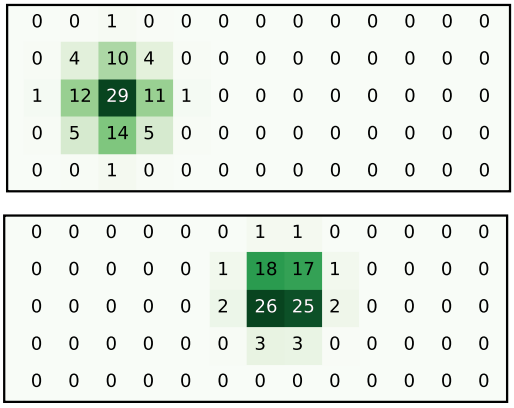

FIG. 4. Fluorescence from individual atoms resolved by ICA. Numbers are the percentage of normalized signal received by that pixel. ICA results for ROI#0(upper) and #2(lower) are shown.

By taking images with the shutter closed, the unavoidable CIC and ADC noise level of the camera is found to have a standard deviation of ~ 5 photo-electrons. The effect of environmental noise sources such as room lights, probe scattering from surfaces, and fluorescence from untrapped background atoms are minimized by a narrow bandpass interference filter and a spatial filter, but still contribute to the background at a combined rate of 29 photo-electrons/ms averaged over the exposure time. Arbitrarily selecting more pixels for ROI will add these noise sources on top of the signal and broaden the histogram peaks, limiting the maximal fidelity. Fluorescence from neighboring sites can contribute to the signal as well. This crosstalk is 2% of the single atom signal per site. For instance with a ~ 150 e^- single atom signal, the neighboring site shows a ~ 3 e^- signal.

IV. DETERMINATION OF REGION OF INTERESTS

In a noise-free detector all pixels that contain signal could be included in the ROI. In practice detector noise prevents this because including more pixels leads to more noise. To maximize Signal-to-Noise Ratio (SNR), a few dominant pixels are chosen for the ROI. Since our trap location is stable, we can set the regions of interests based on high SNR optical molasses imaging. We take several thousand camera shots containing stochastic loading events on five sites. Since atom loading events are uncorrelated we perform independent component analysis (ICA)[4] to infer the locations of the independent emitters. The result of the analysis is shown in Fig. 4. Most of the signal from each site is localized onto 4-5 pixels.

Intrinsic camera noise is uniform over pixels so the number of included pixels determines the noise contribution from the camera. To keep the effect the same at all five sites we choose the same number of pixels at each

site. The maximum number of pixels that gave us non-overlapping ROIs was five, which contained $76-92\%$ of the photo-electron counts based on the ICA.

V. DIPOLE EMISSION PATTERN

The dipole emission pattern is not isotropic, and therefore a simple solid angle estimate based on the lens numerical aperture (NA) is not sufficient. When emitting a circularly polarized photon, the emission pattern is that of a rotating dipole. The fraction of light collected by a lens with numerical aperture NA is:

$$\mathrm{CE} = \int_{\theta_i}^{\theta_f} \int_{-\phi_0}^{\phi_0} \frac{3}{16\pi} \left(\cos^2\theta + 1\right) d\phi \sin\theta d\theta \qquad (6)$$

where CE denotes collection efficiency, θ is polar angle from the atom's quantization axis and ϕ is azimuthal angle. For a lens with a given NA, $\theta_i = \frac{\pi}{2} - \arcsin(\mathrm{NA})$, $\theta_f = \frac{\pi}{2} + \arcsin(\mathrm{NA})$, $\phi_0 = \arcsin\left(\sqrt{\frac{\mathrm{NA}^2}{\sin^2\theta} - \frac{1}{\tan^2\theta}}\right)$. In our configuration, the quantization axis makes an angle α with the optical axis of collection. Therefore in the lens' spherical coordinates the integrand in parentheses becomes

$$\cos^2\theta \rightarrow \left[\cos(\alpha)\cos(\theta) - \sin(\alpha)\sin(\theta)\cos(\phi)\right]^2 \qquad (7)$$

In our setup $\alpha = 60^\circ$ and NA $= 0.40$, which yields a collection efficiency of CE $= 3.94\%$ which is slightly less than for the case of isotropic emission which would give CE $= 4.17\%$.

VI. OPTIMIZATION OF LIGHT POLARIZATION

Standard dielectric cube polarizing beam splitters (PBSs) are used to set a linear polarization, and a pair of $\lambda/4$, and $\lambda/2$ retarders map the linear polarization to circular. Although in principle a $\lambda/4$ retarder is sufficient to map linear polarization to circular, we found that the use of an extra $\lambda/2$ retarder provided better adjustability leading to higher polarization quality. The quality is characterized by a rotating polarizer followed by a photodetector after the beam passes through the vacuum cell. Circularly polarized light transmits regardless of the PBS orientation, while linear polarization does not. Qualitatively the more circular the light is, the smaller the oscillation amplitude as the detection polarizer is rotated. The retarders are rotated to minimize the amplitude of the oscillation. The contrast ratio of the visibility for maximally linear and maximally circular polarizations is used to quantify the purity of the polarization. Assume the polarization state has equal magnitude Cartesian components $E_x = E_y = E_0$ with a finite phase difference ϕ, represented as $\boldsymbol{E} = \left[E_0,\ E_0 e^{i\phi}\right]$ the intensity after passing through the rotating PBS is

$$I(\phi,\theta)/I_0 = \frac{1}{2}\left[1 + \cos(\phi)\sin(\theta)\right] \qquad (8)$$

where θ represents the rotation angle of the PBS. The amplitude of the modulation is $\cos(\phi)/2$ which determines the relative phase. We now decompose the original electric field $\boldsymbol{E}$ into σ_+ and σ_- as $E_{\sigma_+} = \left[\frac{1}{\sqrt{2}},\ -\frac{i}{\sqrt{2}}\right]\cdot\boldsymbol{E}$, $E_{\sigma_-} = \left[\frac{1}{\sqrt{2}},\ \frac{i}{\sqrt{2}}\right]\cdot\boldsymbol{E}$. Therefore the intensity ratio or polarization purity is

$$\frac{I_{\sigma_+}}{I_{\sigma_-}} = \left|\frac{E_{\sigma_+}}{E_{\sigma_-}}\right|^2 = \frac{1+\sin(\phi)}{1-\sin(\phi)} \qquad (9)$$

With the rotating PBS setup, the DC and AC value of the intensity variation can be easily measured. We define the contrast as $C = \frac{\mathrm{DC}}{\mathrm{AC\ amplitude}} = \frac{1/2}{\cos(\phi/2)}$. Then the resulting intensity ratio is

$$\frac{I_{\sigma_+}}{I_{\sigma_-}} = \frac{1+\sqrt{1-1/C^2}}{1-\sqrt{1-1/C^2}} \qquad (10)$$

and can be approximated as $4C^2$ for $C \gg 1$. Using generic polarizing optics we achieve contrasts of $C = 10-20$, corresponding to polarization purities of 400-1600. Higher grade optics can readily improve the extinction. For example we have observed $C \sim 50$ with Glan-Taylor polarizers corresponding to 10^4 polarization purity.

VII. MAGNETIC FIELD OPTIMIZATION

The magnetic field must be closely matched to the probe light polarization. We adapt a procedure from reference [5], which uses the atoms to optimize the magnetic field vector, which defines the quantization axis $\hat{z}$, to coincide with $\vec{k}_{\mathrm{RO}}$ defined by the propagation vector of the probe light. The atoms are first optically pumped to $|F=2, m_F=2\rangle$ by a weak, circularly polarized, unidirectional beam with $B_z \sim 5$ G. One of the σ_+-polarized probe lasers is tuned to $|2\rangle \leftrightarrow |2'\rangle$ and optically pumps the atoms into the $|2,2\rangle$ dark state. When the alignment is optimal, the $|2,2\rangle$ state is nearly dark and can only couple off-resonantly to $|3',3'\rangle$, so depumping to $|1\rangle$ is minimized. If there is any mismatch, the dark state mixes with the bright states and scatters photons, eventually depumping into $|1\rangle$, which can be measured by the destructive blow away measurement. The growth in time of $|D\rangle = |1\rangle$ as a function of the depumping light $|2\rangle \rightarrow |2'\rangle$ quantifies the quality of the alignment, see Fig. 5. The depumping time constants can be compared by preparing $|2,-2\rangle$ using the other MOT σ_- beam, and repeating the sequence. The ratio between the time constants can be used as a figure of merit for the alignment. We measure a ratio ~ 330 as seen from Fig. 5

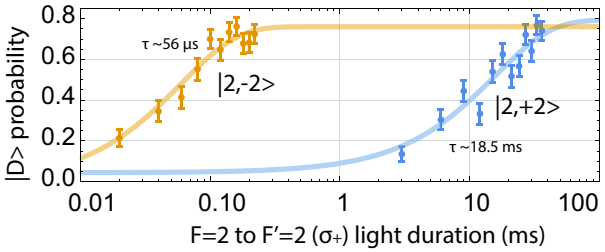

FIG. 5. Growth of the probability of being depumped to the dark state ($F = 1$) for two different stretched Zeeman states $|2, +2\rangle$ (blue) and$|2, -2\rangle$ (yellow). The incident probe is unidirectional σ_+, tuned to the center of the transition $|2, 0\rangle \rightarrow |2', 0'\rangle$ under bias field ~ 5 G.

VIII. TRANSIENT DEPUMPING

When starting from the non-stretched state a higher depumping rate is expected until the atom has been pumped into $|2, 2\rangle$, since σ_+ polarized light can off-resonantly couple $M_F \neq 2$ states to $|2'\rangle$. On average the amount of depumping will be very similar to what is expected for atoms prepared in $M_F = 0$ states, so our experimental results are representative of measurements of qubit states. A numerical simulation to estimate this source of error has been performed using our experimental parameters: $s_0 \sim 1$, $\delta/2\pi = -3$ MHz from the Zeeman shifted cycling transition at $B_z = 20$ G, with polarization impurity of 6.3×10^{-4}, and equally distributed Zeeman state preparation. The mean number of scattered photons needed to pump into the stretched state is ~ 10. Results are shown in Fig. 6.

The scattering process is a sequence of quantum jumps that can be modeled as a Markov chain with finite state-change probability based on the coupling strength $|\Omega|^2$ and decay branching ratios. The effects from time-dependence of the probe intensity and the ODTs are ignored in the simulation. We see a sharp increase in dark state probability until the light optically pumps the atoms. We note that the transient depumping, which gives an error in state determination, could be eliminated by coherently transferring the atoms from the qubit state $|2, 0\rangle$ to the stretched state $|2, 2\rangle$ using microwave or Raman pulses.

IX. RESONANT AND OFF-RESONANT SCATTERING RATES

The Rabi frequency between a ground state $|n, l, J, F, m_F\rangle$ and an excited state $|n', l', J', F', m'_F\rangle$ is

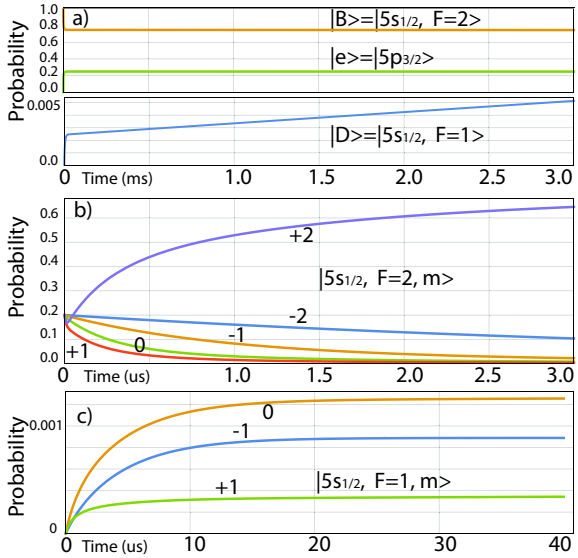

FIG. 6. State dynamics during readout. a) Probability of being in ground hyperfine levels and the excited level. Dark state probability is shown on a different y-scale. b) Transient optical pumping dynamics for the bright state manifold during readout. An initially random $|2, m_F\rangle$ state population is pumped to the stretched state. c) Transient dark state dynamics. Off-resonant coupling to $|2'\rangle$ is possible for all m_F states $m_F \neq 2$, so an increased Raman rate is expected until the atom is in $|2, 2\rangle$.

given by the expression

$$\left|\Omega_{F,m_F}^{F',m_{F'}}\right|^2 = \left(\frac{e\mathcal{E}_q}{\hbar}\right)^2 (2F+1) \times \left|C_{Fm_F1q}^{F'm'_F} \begin{Bmatrix} J & I & F \\ F' & 1 & J' \end{Bmatrix} \langle n'l'J' \| r \| nlJ \rangle\right|^2 \tag{11}$$

where $q = m_{F'} - m_F$, $C_{Fm_F1q}^{F'm_{F'}}$ is a Clebsch-Gordon coefficient, and $\{\}$ is a Wigner 6j symbol. Spherical component q of the optical field is $E_q = \frac{\mathcal{E}_q}{2} e^{-\imath\omega t} + c.c.$. Only coupling to $5p_{3/2}$ is considered due to the large fine structure splitting between $5p_{1/2}$ and $5p_{3/2}$. This allows the couplings to be expressed in terms of the common reduced matrix element $\langle 5p_{3/2} \| r \| 5s_{1/2} \rangle$.

Using the normal scattering rate equation for a two-level system, the scattering rate for each specific transition and polarization can be written as:

$$r_{F,m_F}^{F',m_{F'}} = \frac{\gamma}{2} \frac{\frac{2|\Omega|^2}{\gamma^2}}{1 + \frac{4\delta^2}{\gamma^2} + \frac{2|\Omega|^2}{\gamma^2}}\Bigg|_{\Omega=\Omega_{F,m_F}^{F',m_{F'}}}. \tag{12}$$

Atoms excited to $|F'\rangle$ levels can spontaneously decay to $|F\rangle$ with branching ratio given by:

$$b_F^{F'} = (2J'+1)(2F+1) \left| \begin{Bmatrix} J & I & F \\ F' & 1 & J' \end{Bmatrix} \right|^2, \tag{13}$$

which satisfies the normalization condition $\sum_F b_F^{F'} = 1$.

After a single photon absorption-emission cycle of the bright state, the two possibilities are to decay back to $|B\rangle$ by a resonant process or to $|D\rangle$ by an off-resonant Raman process. In the following sections the relative strength between the cycling transition and the leakage into $|D\rangle$ is calculated for the cases of unpolarized and circularly-polarized probe light.

A. Unpolarized illumination

For the case of probing Zeeman degenerate atoms with unpolarized probe light, the rates for resonant and off-resonant processes are obtained by summing over the scattering rate weighted by the branching ratios with initial ground level $F_i = 2$ and final levels $F_f = 2$ or 1.

$$r_{i\to f} = \sum_{F',m_{F'}} \sum_{m_{F_i}} r_{F_i,m_{F_i}}^{F',m_{F'}} b_{F_f}^{F'} \tag{14}$$

We will denote the resonant process $r_c = r_{2\to 2}$ and the off-resonant process as $r_R = r_{2\to 1}$. From the relative rate of both processes, we obtain a probability to depump for each scattered resonant photon $\beta = r_R/r_c$. Alternatively, we can express the rate in terms of the mean number of emitted photons before a depumping event as: $N_\gamma = 1/\beta$. For near-resonant light $\delta \ll \delta_{2'-3'}$ we obtain the approximate expression for N_γ:

$$N_\gamma = \frac{38340}{1 + 4\delta^2/\gamma^2 + s_0}, \tag{15}$$

where δ is the probe detuning from the $2-3'$ transition, $s_0 = I/I_s$ and $I_s = 3.58\ \mathrm{mW/cm^2}$.

B. Circularly-polarized illumination

For the case of Zeeman non-degenerate atoms and circularly polarized probe light, the probe optically pumps atoms into the stretched state $|2,2\rangle$ where most of the scattering events take place. After the initial fast optical pumping, we can simplify the model to only consider transitions accessible from $|2,2\rangle$. The dominant transition will be the cycling transition $|2,2\rangle \to |3',3'\rangle$ by design. The other transitions are only accessible due to polarization and alignment imperfections, which open off-resonant transitions to $|2',2'\rangle$, $|2',1'\rangle$ and $|1',1'\rangle$. Since transitions to $|3',m'_F \neq 3'\rangle$, will scatter only to $|2\rangle$ and be pumped back to $|2,2\rangle$, these states can be ignored in this analysis.

To see the influence and sensitivity of polarization and alignment errors, we parametrize the polarization purity by the intensity fraction $(\epsilon_{-1}, \epsilon_1) = (1-p, p)$ where ϵ_q denotes the fraction of spherical component q and $0 \le p \le 1$. The angular mismatch between the quantization-axis $\hat{z}$ and $\vec{k}_{\mathrm{RO}}$ is represented by the angle θ. An angular mismatch θ projects the circular polarization to the z axis, allowing coupling to $\Delta m_F = 0$ transitions. For a given polarization purity and angular mismatch, one can calculate the projection using the Wigner-D function for a spin-1 particle. The perfectly matched case gives a projection $(w_{-1}, w_0, w_{+1})=(1-p, 0, p)$ where $\sum_{q=-1}^{1} w_q = 1$. If θ is small, the resonant process rate r_c can be written as

$$\begin{aligned} r_c &= r_{2,2}^{3',3'}(w_{+1}) \\ &\equiv \frac{\gamma}{2} \frac{s_0 \left[p(D^1_{1,1}(\theta))^2 + (1-p)(D^1_{-1,1}(\theta))^2\right]}{1 + \frac{4\delta^2}{\gamma^2} + s_0 \left[p(D^1_{1,1}(\theta))^2 + (1-p)(D^1_{-1,1}(\theta))^2\right]} \end{aligned} \tag{16}$$

where $D^j_{m_1,m_2}(\theta)$ is the Wigner-D function and for the following derivation, they are explicitly written. Here $s_0 = I/I_{s,c}$, and $I_{s,c} = 1.66\ \mathrm{mW/cm^2}$. Raman processes can occur via coupling to $|2',2'\rangle$ by π-projection and to $|2',1'\rangle$ and $|1',1'\rangle$ by σ_- projection. Considering the branching ratios to the dark state, the Raman rate r_R is

$$r_R = \left[r_{2,2}^{2',2'}(w_0) + r_{2,2}^{2',1'}(w_{-1})\right] b_1^{2'} + r_{2,2}^{1',1'}(w_{-1}) b_1^{1'} \tag{17}$$

Neglecting saturation effects on $2 \leftrightarrow 2'$ and $2 \leftrightarrow 1'$ transitions, we can simplify the denominators and obtain

$$\begin{aligned} r_R \simeq \frac{\gamma}{2}\frac{1}{2} &\left[\frac{s_0}{3}\left(p\sin^2\frac{\theta}{2} + (1-p)\cos^2\frac{\theta}{2}\right)\right. \\ &\left. + \frac{s_0}{6}\left((1-p)\cos^4\frac{\theta}{2} + p\sin^4\frac{\theta}{2}\right)\right] \\ &/\left(1 + \frac{4\delta^2_{2'-3'}}{\gamma^2}\right) \\ &+ \frac{\gamma}{2}\frac{5}{6}\left[\frac{s_0}{6}\frac{(1-p)\cos^4\theta/2 + p\sin^4\theta/2}{1 + \frac{4\delta^2_{1'-3'}}{\gamma^2}}\right] \end{aligned} \tag{18}$$

where $\delta_{2'-3'}, \delta_{1'-3'}$ are excited state hyperfine splittings. The denominators can be further simplified at large detuning, yielding

$$r_R = \frac{\gamma s_0}{2} f(\theta, p) \tag{19}$$

where

$$\begin{aligned} f(\theta,p) = \frac{\gamma^2}{48\delta^2_{2'-3'}} &\left[2\left(p\sin^2\frac{\theta}{2} + (1-p)\cos^2\frac{\theta}{2}\right)\right. \\ &\left. + \left((1-p)\cos^4\frac{\theta}{2} + p\sin^4\frac{\theta}{2}\right)\right] \\ &+ \frac{5\gamma^2}{144\delta^2_{1'-3'}}\left[(1-p)\cos^4\theta/2 + p\sin^4\theta/2\right]. \end{aligned} \tag{20}$$

Again, taking the relative rate r_c/r_R gives the mean number of photons the bright state can scatter before one

depumping event. This can be approximated by:

$$N_{\gamma,\sigma}(\theta,p) \simeq \frac{p\cos^4\frac{\theta}{2}}{p\sin^4\frac{\theta}{2}+\sin^2\frac{\theta}{2}+(1-p)\cos^4\frac{\theta}{2}} \times \left(\frac{7}{4}\right)\left[\frac{38340}{1+4\delta^2/\gamma^2+s_0}\right]. \quad (21)$$

valid when $\theta \ll 1$, $\delta \ll \delta_{2'-3'}$, $p \sim 1$. For the perfectly aligned case $\theta = 0$, depumping is suppressed by a factor of $\frac{4}{7}\frac{1-p}{p}$. Under non-zero magnetic field and optical potential one should include state dependent Zeeman and AC stark shifts in order to obtain more accurate results.

X. FICTITIOUS MAGNETIC FIELD

Consider the AC stark shift ΔE_ψ of an atom in state $|\psi\rangle$ illuminated by a single frequency optical field ω written as

$$\Delta E_\psi = -\frac{1}{4}\alpha_\psi(\omega)\mathcal{E}^2 \quad (22)$$

where α_ψ is the dynamic polarizability which can be decomposed into scalar($\alpha_\psi^{(0)}$), vector($\alpha_\psi^{(1)}$) and tensor($\alpha_\psi^{(2)}$) contributions as

$$\alpha_{nJF}(\omega) = \alpha^{(0)}_{nJF}(\omega) + \mathcal{A}(\hat{k}\cdot\hat{z})m_F\alpha^{(1)}_{nJF}(\omega) + \left[\frac{3(\hat{p}\cdot\hat{z})^2-1}{2}\right]\frac{3m_F^2-F(F+1)}{F(2F-1)}\alpha^{(2)}_{nJF}(\omega). \quad (23)$$

Here $\mathcal{A}$ represents the circularity of light ranging continuously from 1(Right handed) to -1(Left handed), and 0 for linear polarization. Unit vectors $\hat{k}, \hat{p}$ and $\hat{z}$ denote the orientations of wave vector, electric field and quantization axis defined by the bias magnetic field.

The effect of a vector light shift is equivalent to having a static magnetic field $B_{\rm fict}$. We obtain an equivalent field by equating the shift to Zeeman shifts

$$-\frac{1}{4}\mathcal{A}m_F\alpha^{(1)}_{nJF}\mathcal{E}^2\hat{k} = \mu_B g_{nJF} m_F \vec{B}_{\rm fict} \quad (24)$$

the equivalent fictitious field is given by:

$$\vec{B}_{\rm fict} = -\frac{\mathcal{A}\alpha^{(1)}}{4\mu_B g_{nJF}}\mathcal{E}^2\hat{k} \quad (25)$$

with Landé g-factor g_{nJF}.

It is convenient to express the shift in terms of the mean trap depth for ground states as $U_{\rm trap} = -1/4\alpha^{(0)}_{5s_{1/2}}\mathcal{E}^2$

$$\vec{B}_{\rm fict} = \frac{U_{\rm trap}}{\mu_B g_{nJF}}\left[\frac{\mathcal{A}\alpha^{(1)}_{5s_{1/2}}}{\alpha^{(0)}_{5s_{1/2}}}\right]\hat{k} \quad (26)$$

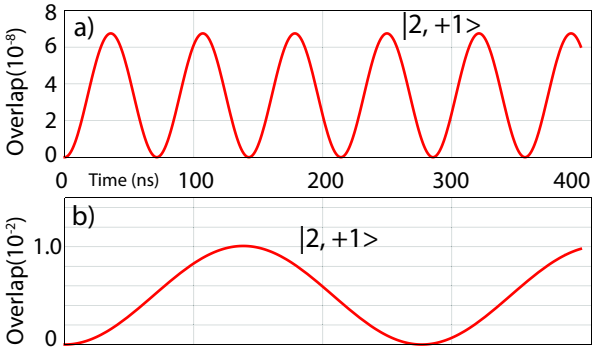

FIG. 7. (color online) Larmor precession of $|2,+2\rangle$ showing finite overlap to $|2,+1\rangle$. a) For our experimental configuration: $\alpha = 60^\circ$,$B_{ext} = 20$G, $B_{fict} = 3$mG. b) Experiment configuration with more fictitious field. $B_{ext} = 5$G, $B_{fict} = 0.3$G. Both cases have negligible overlap to $m = -2, -1, 0$.

The equation gives both magnitude and orientation of the fictitious magnetic field. With finite circularity of the ODT light the bright state experiences

$$\frac{d\vec{B}_{\rm fict}}{dU_{\rm trap}} = 29.77\left[\frac{\mathcal{A}\alpha^{(1)}_{5s_{1/2}}}{\alpha^{(0)}_{5s_{1/2}}}\right]\hat{k} \quad \text{G/mK} \quad (27)$$

where we have expressed the trap depth in temperature units.

The impact of this extra field is an effective time-dependent magnetic field during the 6 ms interrogation stage. While atoms are being probed, the traps are off and they are continuously pumped and projected to the stretched state, $|2,2\rangle$ along the quantization axis $\hat{z}$ originally set by the external static magnetic field $\vec{B}_{\rm ext}$. When the traps are turned back on, $\vec{B}_{\rm ODT} = \vec{B}_{\rm ext} + \vec{B}_{\rm fict}$ sets the quantization axis, and if these two axes are not parallel, $|2,2\rangle$ is no longer an eigenstate. The state $|2,2\rangle$ will undergo Larmor precession about the new axis with the frequency $\omega_L = \mu_B g_F B_{\rm ODT}/\hbar$. The projection onto other Zeeman states in a rotated frame can be calculated from the Wigner-D function for a spin-2 particle. If the atom is projected to a non-stretched state when the next probe cycle begins, it will go through another optical pumping cycle and experience a temporarily increased depumping rate to $|D\rangle$.

To estimate the contribution of this effect to depumping let us begin with the initial stretched state $|2,2\rangle$ and have it precess under magnetic field $\vec{B}_{\rm ODT}$, governed by the Hamiltonian $H = \mu_B g_F \vec{F}\cdot\vec{B}_{\rm ODT}$ where $\vec{F}$ is the angular momentum operator. The angle θ_0 between $\vec{B}_{\rm ext}$ and the new field $\vec{B}_{\rm ODT}$ is

$$\theta_0 = \arctan\left(\frac{x\sin\alpha}{1+x\cos\alpha}\right) \quad (28)$$

where α is the angle between $\vec{B}_{\rm ext}$ and $\vec{B}_{\rm fict}$ and $x \equiv B_{\rm fict}/B_{\rm ext}$ is the relative strength of the fields. For small

axis mismatch, precession couples the closest m state, $|2,2\rangle \leftrightarrow |2,1\rangle$. Projection to the $m_F = 1$ state is time-dependent and dictated by the Larmor frequency. We consider maximal overlap to estimate maximal depumping due to the fictitious field.

$$\left|\langle 2,1|\, e^{\frac{-iHt}{\hbar}}\, |2,2\rangle\right|^2 \leq \left|D^2_{2,1}(2\theta_0)\right|^2 = 4\cos^6\theta_0 \sin^2\theta_0 \tag{29}$$

Substituting θ_0 obtained from Eq. (28) shows the overlap is bounded by

$$\left|\langle 2,1|\, e^{\frac{-iHt}{\hbar}}\, |2,2\rangle\right|^2 \leq \frac{4x^2\left(1 + x\cos^6\alpha\right)\sin^2\alpha}{\left(1 + x^2 + 2x\cos\alpha\right)^4}. \tag{30}$$

For small vector shift ($x \ll 1$), the expression reduces to $\leq 4x^2\sin^2(\alpha)$ showing a quadratic dependency. For our experiment, the vector light shift makes an angle $\alpha = 60°$, and the relative strength of the fields x is 1.5×10^{-4}. These parameters give the maximal projection of precessed stretched state to the neighboring m-state to be 6.7×10^{-8} per cycle, which agrees with the numerical simulation shown in Fig.7a). What this means is that when the precessed state is illuminated by the light again, it has a probability of being projected to the $m_F = 1$ state of at most that number. Since we repeat the 800 ns long chopping cycle for 6 ms, $\sim$ 7500 projections will occur. Multiplying with 7500 gives an expected number of m-changing scattering events 5.1×10^{-4} per readout, and each readout scatters $\sim 10^4$ photons. Therefore the vector light shift induced depumping is equivalent to having polarization contamination at the $\sim 10^{-8}$ level, orders of magnitude smaller than our measured contamination. This agrees with our observation that we failed to observe trap intensity dependent depumping, once the circularity in the ODT light was reduced from the parameters in Fig 7b).

[1] I. I. Beterov and M. Saffman, "Rydberg blockade, Förster resonances, and quantum state measurements with different atomic species," Phys. Rev. A **92**, 042710 (2015).

[2] T. Xia, M. Lichtman, K. Maller, A. W. Carr, M. J. Piotrowicz, L. Isenhower, and M. Saffman, "Randomized benchmarking of single-qubit gates in a 2D array of neutral-atom qubits," Phys. Rev. Lett. **114**, 100503 (2015).

[3] M. Hirsch, R. J. Wareham, M. L. Martin-Fernandez, M. P. Hobson, and D. J. Rolfe, "A stochastic model for electron multiplication charge-coupled devices from theory to practice," PLOS ONE **8**, 1–13 (2013).

[4] A. Hyvärinen and E. Oja, "Independent component analysis: algorithms and applications," Neural Netw. **13**, 411 – 430 (2000).

[5] M. Martínez-Dorantes, *Fast non-destructive internal state detection of neutral atoms in optical potentials*, Ph.D. thesis, Rheinischen Friedrich-Wilhelms-Universität Bonn (2016).